Numerical modelling of quasi-brittle fracture with the rate-dependent multiple embedded discontinuity approach

Timo Saksala

Summary. This article deals with 2D numerical modelling of fracture in quasi-brittle materials. For this end, a rate-dependent multiple embedded discontinuity model is developed to simulate quasi-brittle fracture within the finite elements context. In the present modification of the embedded discontinuity approach, the discontinuities are pre-embedded (before the analysis) into each finite element of the mesh. With the chosen constant strain triangle element, this results in three discontinuity lines each oriented parallel to the sides of the triangle element. Each discontinuity line has its own displacement jump and loading surface. The displacement jumps and elemental stresses are simultaneously solved with the multisurface plasticity techniques. Rate-dependency is incorporated with the viscoplastic consistency approach. The global equations of motion are solved in time by explicit time integration. The model performance is demonstrated in numerical examples where the uniaxial tension and compression tests are simulated.

In memory of Professor Juhani Koski

Introduction

Numerical modelling of quasi-brittle fracture has been gaining increasing interest during the last few decades due to its importance in many fields of engineering, such as concrete structures and geotechnical analyses. Many numerical codes based on the finite element and the discrete element methods have been developed to simulate the brittle fracture. For a review on computational methods for fracture in brittle and quasi-brittle solids, see [1]. The major challenge in such analyses is the numerical modelling of crack propagation.

A promising numerical technique to describe crack propagation is the embedded discontinuity approach [2-5]. These techniques allow either a strain (weak) or displacement (strong) discontinuity inside a finite element. This is achieved by

enhancement of the strain or displacement field in order to capture the discontinuity. Saksala [6] successfully applied this method for numerical modelling of rock fracture.

A close relative of this method is the extended finite element method (XFEM) which enriches the element interpolation (nodal) basis by exploiting the partition of unity property [7]. However, the embedded discontinuity approach is chosen in this paper because it has a computational advantage over the XFEM due to the completely local nature of the required enhancements while offering the same kind of accuracy and convergence. Particularly, the additional degrees of freedom, representing the displacement or strain jump, can be eliminated by static condensation. Moreover, the additional degrees of freedom are global in the XFEM and thus increase during the propagation of discontinuity.

In the usual application of the embedded discontinuity method for quasi-static analyses, single embedded discontinuity (a crack) with a normal parallel to the first principal direction of the stress tensor is introduced (during the analysis) into a finite element when the first principal stress exceeds the tensile strength of the material. A variant implementation based on multiple or intersecting discontinuities embedded successively parallel to element facets (edges) is proposed in [8]. Multiple discontinuities approach effectively alleviates the stress locking and spreading problems typical for embedded discontinuity approach, as shown in [9, 10]. The implementation of multiple discontinuities parallel to element edges is similar to the classical interface or cohesive zone elements method but considerably simpler and computationally more efficient as neither cohesive zone elements requiring duplication of mesh nodes nor contact interfaces are needed upon closing cracks.

In the present paper, a modification of the multiple discontinuities approach where the discontinuities are embedded before the analysis parallel to the edges of the constant strain element (CST) is presented and applied to simulation of rock fracture. Each discontinuity has its own rate dependent loading surface so that the computational multisurface techniques can be employed in solving for the displacement jumps and element stresses. Rate-dependency is introduced for numerical stability reasons with the viscoplastic consistency approach. The model performance is demonstrated in 2D numerical examples of rock compression and tension tests solving the equations of motion explicitly in time.

Theory of the model

The theory of the present model is presented in this section. First, the strong discontinuity kinematics is briefly described. Then, the finite element implementation of the embedded discontinuity kinematics is presented. Finally, the multiple embedded discontinuity model is summarized and the solution method for the displacement jumps is outlined.

Strong discontinuity kinematics

A body occupying domain Ω in $\mathbf{R}^2$ with a boundary $\partial\Omega$ (see Figure 1) is split into two disjoint parts Ω^+ and Ω^- by a strong discontinuity line Γ_d defined by its normal $\mathbf{n}$ and

tangent $\mathbf{m}$. The displacement and strain field (assuming infinitesimal deformation) can

$$\mathbf{u}(\mathbf{x}) = \overline{\mathbf{u}}(\mathbf{x}) + \underbrace{\left(H_{\Gamma_d}(\mathbf{x}) - \varphi(\mathbf{x})\right)\overline{\overline{\mathbf{u}}}(\mathbf{x})}_{M_{\Gamma_d}(\mathbf{x})}$$

$$\boldsymbol{\varepsilon}(\mathbf{x}) = \nabla^s \overline{\mathbf{u}}(\mathbf{x}) - (\overline{\overline{\mathbf{u}}}(\mathbf{x}) \otimes \nabla\varphi(\mathbf{x}))^{sym} + \delta_{\Gamma_d}(\mathbf{x})(\overline{\overline{\mathbf{u}}}(\mathbf{x}) \otimes \mathbf{n})^{sym}$$

(1)

be decomposed as a function of the location $\mathbf{x} \in \Omega$ as
where ∇^s is "the symmetric part of the gradient" operator, $\overline{\mathbf{u}}(\mathbf{x})$ represents the displacement field without the discontinuity, $\overline{\overline{\mathbf{u}}}(\mathbf{x})$ is the displacement jump at Γ_d due to discontinuity, and $H_{\Gamma_d}(\mathbf{x})$ is the Heaviside function at the discontinuity. Function $\varphi(\mathbf{x})$ is defined in a subdomain $\Omega_\varphi = \Omega_\varphi^+ \cup \Omega_\varphi^-$ so that $\varphi(\mathbf{x}) = 0$ when $\mathbf{x} \in \Omega^- \setminus \Omega_\varphi^-$, $\varphi(\mathbf{x}) = 1$ when $\mathbf{x} \in \Omega^+ \setminus \Omega_\varphi^+$ (with \ signifying the set theoretic difference), and it is C^0-continous between 0 and 1 when $\mathbf{x} \in \Omega_\varphi$. The reason for using the decomposition in (1), instead of the natural one with $\varphi(\mathbf{x}) \equiv 0$, is that both $\overline{\mathbf{u}}(\mathbf{x})$ and $\overline{\overline{\mathbf{u}}}(\mathbf{x})$ may be nonzero at the boundary $\partial\Omega$ which means that their effect should be taken into consideration in the finite element context when imposing the essential boundary conditions. It is more convenient to use decomposition (1), as function $M_{\Gamma_d}^e(\mathbf{x})$, appearing in Equation (1), restricts the effect of the displacement jump to subdomain Ω_φ.
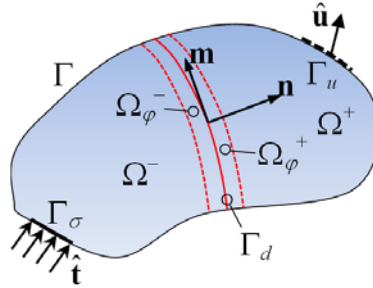

Figure 1. Domain crossed by a discontinuity line.

Moreover, the result $\nabla H_{\Gamma_d} = \delta_{\Gamma_d}\mathbf{n}$ on Dirac delta function δ_{Γ_d} and constant displacement jump assumption yielding $\nabla^s\overline{\overline{\mathbf{u}}} = \mathbf{0}$ were used in the derivation of the strain in (1).

Finite element implementation of strong discontinuity kinematics

As the body in Figure 1 is discretized with the CST elements, the embedded discontinuity becomes a straight line (inside an element) as is illustrated in Figure 2. The FE version of Equation (1) reads

$$\mathbf{u} = N_i\mathbf{u}_i^e + \underbrace{\left(H_{\Gamma_d} - N^{sol}\right)\boldsymbol{\alpha}_d}_{M_{\Gamma_d}^e}$$

$$\boldsymbol{\varepsilon} = \underbrace{(\nabla N_i \otimes \mathbf{u}_i^e)^{sym}}_{\overline{\varepsilon}} - \underbrace{(\nabla N^{sol} \otimes \boldsymbol{\alpha}_d)^{sym} + \delta_{\Gamma_d}(\mathbf{n} \otimes \boldsymbol{\alpha}_d)^{sym}}_{\overline{\overline{\varepsilon}}}$$

(2)

where the displacement jump is denoted by $\boldsymbol{\alpha}_d$, while N_i and $\mathbf{u}_i^e$ are the standard (linear with CST) interpolation functions and nodal displacements ($i = 1,2,3$ with summation on repeated indices), respectively. It is noted that the dependency of the quantities on the placement vector, $\mathbf{x}$, in Equation (1) and henceforth are omitted for brevity of notations.
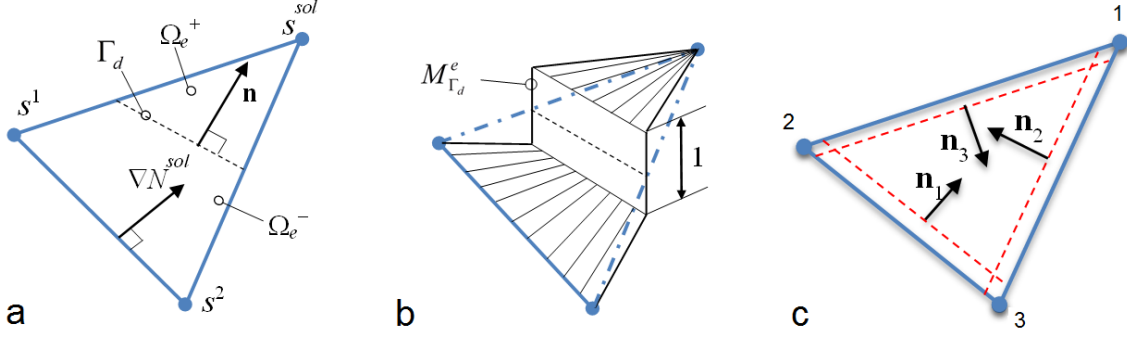

Figure 2. CST element with a discontinuity line (a), function $M_{\Gamma_d}^e$ (b), and three discontinuities parallel to element sides (c).

Thus, in the finite element context function φ in Equation (1) is identified with the interpolation function N^{sol} related to the solitary node, s^{sol}, with its support being a single element. Finally, it is noted that according to the enhanced assumed strains (EAS) concept, the terms comprising the discretized strain can be identified as the compatible part $\bar{\boldsymbol{\varepsilon}}$ and the enhanced part $\bar{\bar{\boldsymbol{\varepsilon}}}$ [8].

The FE discretized version of the weak form of the balance of linear momentum can be obtained by standard arguments and is not shown here. The variation of the enhanced part of the strain (see Equation (2)) is based on the EAS concept where the enhanced modes are constructed in the strain space, orthogonal to the stress field. Applying the EAS concept and the Petrov-Galerkin formulation, the variation of the enhanced strain and the L_2-orthogonality condition can be written as [8]

$$\delta\bar{\bar{\boldsymbol{\varepsilon}}} = -\frac{1}{A_e}(\boldsymbol{\beta}_d \otimes \mathbf{n})^{sym} + \frac{1}{l_d}(\boldsymbol{\beta}_d \otimes \mathbf{n})^{sym}\delta_{\Gamma_d}$$

$$\int_{\Omega_e} \delta\bar{\bar{\boldsymbol{\varepsilon}}} : \boldsymbol{\sigma}d\Omega = 0 \tag{3}$$

where $\boldsymbol{\beta}_d \in \mathbf{R}^2$ denotes an arbitrary variation of the displacement jump, A_e is the area of a finite element, and l_d is the length of a discontinuity. Substitution of $\delta\bar{\bar{\boldsymbol{\varepsilon}}}$ into the second equation in Equation (3) gives, after some manipulations

$$\frac{1}{A_e}\int_{\Omega_e \backslash \Gamma_d} \boldsymbol{\sigma} \cdot \mathbf{n}d\Omega = \frac{1}{l_d}\int_{\Gamma_d} \mathbf{t}_{\Gamma_d} d\Gamma_d = \mathbf{0} \tag{4}$$

With the CST element this equation – representing essentially a weak form of traction continuity – becomes also the local (strong) form of traction continuity, i.e. $\mathbf{t}_{\Gamma_d} = \boldsymbol{\sigma} \cdot \mathbf{n}$,

since the integrands in Equation (4) are constants. This EAS concept based formulation provides a very simple implementation where neither the explicit position of the discontinuity line within the element nor its length is necessary to be known.

Rate dependent multiple embedded discontinuity model

A three-surface intersecting discontinuity model is presented here. As mentioned in Introduction, the discontinuities are placed into each element of the mesh parallel to element sides, as illustrated in Figure 2c. Thereby, the unit normal for each discontinuity is calculated as

$$\mathbf{n}_i = \frac{\nabla N_i}{\| \nabla N_i \|} \quad (i = 1,2,3 \text{ with no summation on } i) \tag{5}$$

where N_i is the interpolation function of node i. The single discontinuity kinematics can be extended in a straightforward manner to the multiple discontinuity case since each discontinuity has its own displacement jump. Thereby, Equation (2) becomes

$$\mathbf{u} = N_i \mathbf{u}_i^e + \sum_{k=1}^{3} \left(H_{\Gamma_d}^k - N_k \right) \boldsymbol{\alpha}_d^k$$

$$\boldsymbol{\varepsilon} = (\nabla N_i \otimes \mathbf{u}_i^e)^{sym} - \sum_{k=1}^{3} \left((\nabla N_k \otimes \boldsymbol{\alpha}_d^k)^{sym} + \delta_{\Gamma_d}^k (\mathbf{n}_k \otimes \boldsymbol{\alpha}_d^k)^{sym} \right) \tag{6}$$

With this expression for strain, the traction vector for each discontinuity i can be written as

$$\mathbf{t}_{\Gamma_d}^i = \boldsymbol{\sigma} \cdot \mathbf{n}_i$$

$$= \left(\mathbf{E} : (\bar{\boldsymbol{\varepsilon}} - \sum_{k=1}^{3} (\nabla N_k \otimes \boldsymbol{\alpha}_d^k)^{sym}) \right) \cdot \mathbf{n}_i \tag{7}$$

with $\mathbf{E}$ being the elasticity tensor. It should be noted that the stress tensor $\boldsymbol{\sigma}$ in (7) is common to all discontinuities in the same element. The loading functions (similar to those in [9]), softening rules and evolution laws for each discontinuity i are defined as

$$\phi_i(\mathbf{t}_{\Gamma_d}^i, \kappa_i, \dot{\kappa}_i) = \mathbf{n}_i \cdot \mathbf{t}_{\Gamma_d}^i + \beta \left| \mathbf{m}_i \cdot \mathbf{t}_{\Gamma_d}^i \right| - (\sigma_t + q_i(\kappa_i, \dot{\kappa}_i))$$

$$q_i = h_i \kappa_i + s \dot{\kappa}_i, \quad h_i = -g \sigma_t \exp(-g \kappa_i), \quad g = \frac{\sigma_t}{G_{Ic}} \tag{8}$$

$$\dot{\boldsymbol{\alpha}}_d^i = \dot{\lambda}_i \frac{\partial \phi_i}{\partial \mathbf{t}_{\Gamma_d}^i}, \quad \dot{\mathbf{t}}_{\Gamma_d}^i = -\mathbf{E} : \sum_{k=1}^{3} (\nabla N_k(\mathbf{x}) \otimes \dot{\boldsymbol{\alpha}}_d^k)^{sym} \cdot \mathbf{n}_i, \quad \dot{\kappa}_i = \dot{\lambda}_i \frac{\partial \phi_i}{\partial q_i} \quad (i = 1,2,3)$$

where $|x|$ denotes the absolute value of scalar x, $\mathbf{m}_i$ denotes the unit tangent of a discontinuity i, $\kappa_i, \dot{\kappa}_i$ are the internal variable and its rate related to the softening law for a discontinuity i, and σ_t and s are the tensile strength and the viscosity of the material. Moreover, h_i is the softening modulus of the exponential softening rule. Parameter g that controls the initial slope of the softening curve is calibrated by the mode I fracture

energy G_{Ic}. Finally, β is a shear control parameter that governs the interaction between the tensile (mode-I) and the shear (mode-II) component of the traction.

The formal similarity of Equation (7) and (8) to plasticity theory enables (after eliminating the rate of the internal variable $\dot{\lambda}_i$) the exploitation of standard computational multisurface plasticity techniques in solving for the displacement jumps and updating the internal variables, see [9]. In particular, the increments of the magnitudes of the displacement jumps $\delta\lambda_i$ can be solved generally as (assuming $\phi_i > 0$ for all $i = 1,2,3$)

$$\mathbf{G}\delta\boldsymbol{\lambda} = \mathbf{F} \quad \text{with}$$

$$G_{ij} = (\frac{\partial\varphi_i}{\partial\mathbf{t}_{\Gamma_d}^i})^T \mathbf{N}_d^i \mathbf{E}\nabla\mathbf{N}_j \frac{\partial\varphi_j}{\partial\mathbf{t}_{\Gamma_d}^j} + \delta_{ij}\left(h_i + \frac{s}{\Delta t}\right), \quad F_i = \phi_i \tag{9}$$

$$\mathbf{N}_d^i = \begin{bmatrix} n_x^i & 0 & n_y^i \\ 0 & n_y^i & n_x^i \end{bmatrix}, \quad \nabla\mathbf{N}_j = \begin{bmatrix} \nabla N_j^x & 0 \\ 0 & \nabla N_j^y \\ \nabla N_j^y & \nabla N_j^x \end{bmatrix}, \quad i,j = 1,2,3$$

where matrix notation is used and n_x^i are n_y^i are the components of $\mathbf{n}_i$. After the increment $\delta\boldsymbol{\lambda}$ is solved, the increments of the displacement jumps, traction vectors and the internal variables are updated according to Equation (8). The new stress state is then calculated according to the definition of stress in Equation (7). It should be noted that the case where the magnitudes of all three displacement jumps are active in the end of the stress integration. i.e. $\Delta\lambda_i = \sum \delta\lambda_i > 0$ $(i = 1,2,3)$, does not actually realize. This follows from the partition unity property of the interpolation functions giving $\sum_{i=1}^3 \nabla N_i = 0$. Thus, only two independent edge modes are possible in 2D [8].

The presented formulation results in a simple computational scheme where the global equations of motion are solved with an explicit time integrator and the local problem for stresses, displacement jumps and internal variables with the elastic-plastic operator split. Finally, it is emphasized that the present model incorporates loading rate sensitivity so that it can be applied in dynamic loading conditions. Moreover, on solving for $\delta\boldsymbol{\lambda}$ the diagonal entries of $\mathbf{G}$ must remain positive. This may become crucial, if the softening curve is extremely steep, i.e. the absolute value of h_i is greater than the stiffness term. Thus, the positivity is secured by the presence of term $s/\Delta t$, which is usually of several orders of magnitude.

Numerical examples

Present model performance is tested in this section both at the material point level using a single element mesh and at the structural level where the uniaxial compression and tension tests on rock like material are simulated. The material properties taken from [10] (valid for Stanstead granite) and model parameters for simulations are given in Table 1.

Table 1. Material properties and model parameters

Quantity	Symbol	Value	Unit
Young's modulus	E	67.3	GPa
Elastic limit stress in tension	σ_t	8.9	MPa
Poisson's ratio	v	0.27	
Material density	ρ	2616	kg/m^3
Mode I fracture energy	G_{Ic}	0.0355	N/m
Viscosity for discontinuity	s	0.001	MPa·s/m
Shear control parameter	β	1	

Material point level tests

Before the laboratory sample level simulations, the model predictions are demonstrated at the material point level in tension. For this end, the model response is tested with the single CST element model and boundary conditions shown in Figure 3.
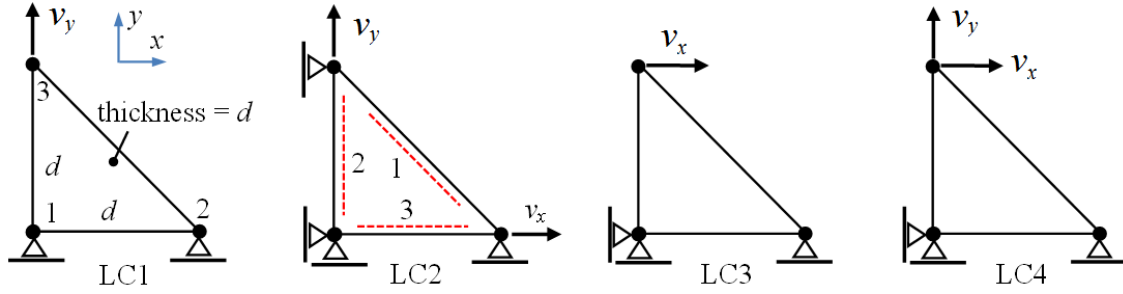

Figure 3. Single element model and boundary conditions for material point level simulations.

The element side length d is set to 10 mm and the magnitude of constant velocity is 0.001 m/s in each load case. The effect of viscosity is tested in LC1 while in other load cases the value given in Table 1 is used. The simulation results are shown Figure 4.
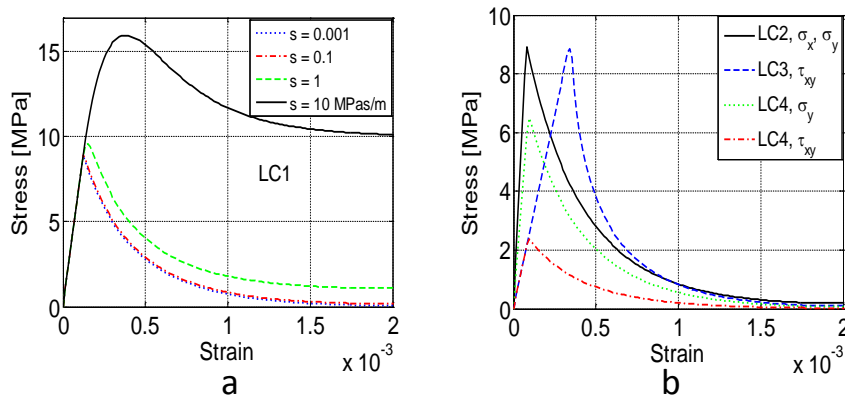

Figure 4. The model predictions at the material point level simulations: effect of viscosity in LC1 (a), and model response in LC2, LC3 and LC4 (b).

The effect of the viscosity modulus on the model response shown in Figure 4a is typical for viscoplasticity models, i.e. the higher the modulus, the higher the peak strength and the more ductile the post-peak behavior. Only crack 3 (shown in Figure 3) opens in LC1. In LC2, the model prediction is naturally identical in both x and y direction as the magnitudes of crack 2 and 3 opening develop equally. When the loading is imposed on node 3 only in x direction (LC3), only the shear stress of the element differs from zero (Figure 3b). In this load case, crack 1 and 2 both open in the beginning of the softening process. However, crack 1 becomes inactive almost immediately so that only crack 2 opening develops during the loading. Finally, in LC4 crack 1 and 3 both open first upon reaching the tensile strength but then almost immediately after only crack 3 opening remains active so that in the end of the softening process, crack 1 opening is only 6.6E-5 mm while that of crack 3 is 0.03 mm.

Laboratory sample level tests

Uniaxial tension and compression tests are simulated here with the model shown in Figure 5 in order to demonstrate the model performance at the laboratory sample level. The material properties and model parameters are those shown in Table 1.
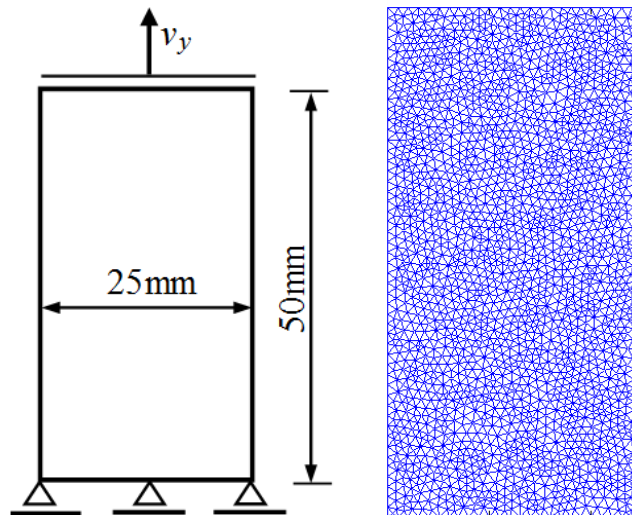

Figure 5. Model, CST mesh (4276 elements), and boundary conditions for uniaxial tension and compression simulations.

The constant velocity boundary condition with v_y = 0.02 m/s in the tension test simulations and v_y = −0.1 m/s in compression is applied here. The simulation results with two different values of the shear control parameter are shown in Figure 6 and 7.
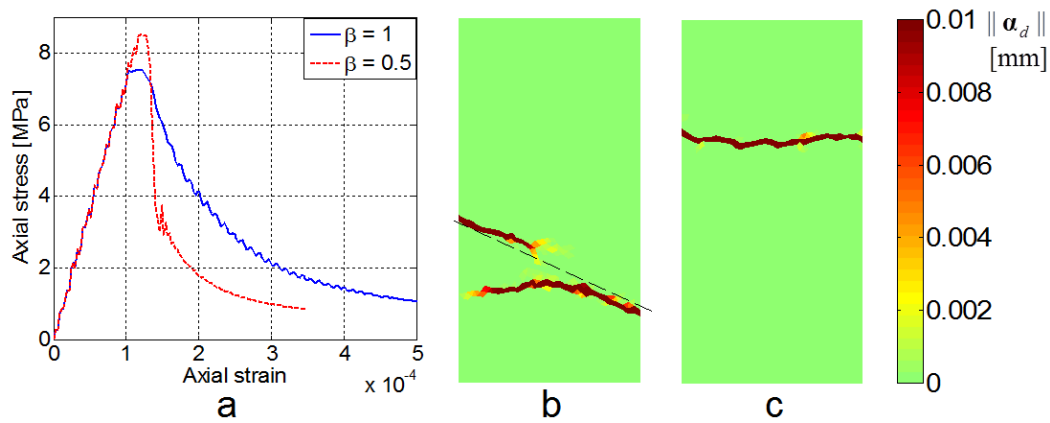
Figure 6. Simulation results for uniaxial tension test: Axial stress vs. strain curves (a), final failure modes with $\beta = 1$ (b), and $\beta = 0.5$ (c).

The final failure modes in Figure 6b and c are presented in terms of the magnitude of the sum of displacement jump vectors norms for each element. The effect of the shear parameter is obvious in the results: value $\beta = 1$ leads to a double crack system with an inclined trend indicated in Figure 6b by a dashed line. When the shear parameter value is decreased to $\beta = 0.5$, the macrocrack is approximately orthogonal to the loading direction, which is the observed case in the experiments for rocks and concrete. With this smaller value of β, the predicted material response is more brittle as well. Finally, the uniaxial compression test results are shown in Figure 7 (the geomechanics convention of regarding compressive stress and strain positive is adopted here).
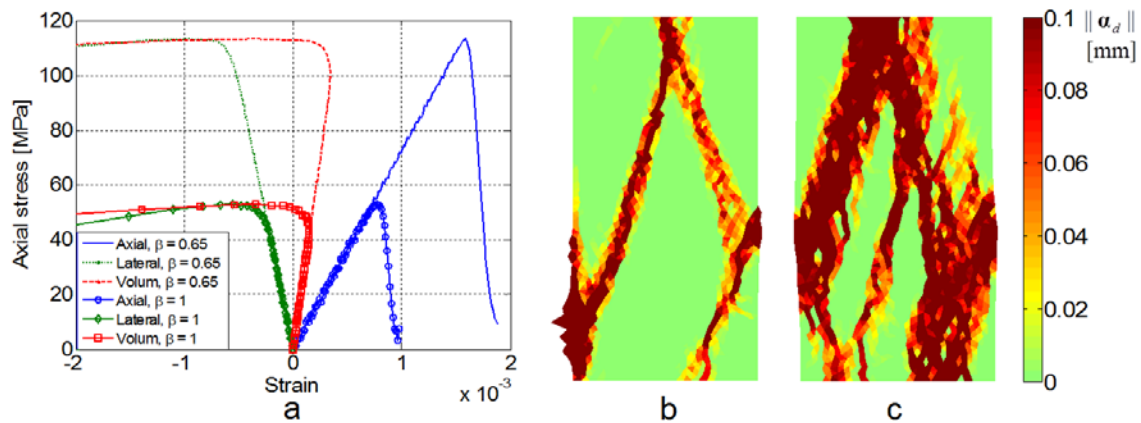

Figure 7. Simulation results for uniaxial compression test: Axial, lateral and volumetric strain vs. axial stress curves (a), final failure modes with $\beta = 1$ (b), and $\beta = 0.65$ (c).

The stress-strain curves in Figure 7a exhibit typical features observed in the experiments of rock under uniaxial compression [10]. Volumetric strain is first compactant but changes then to dilatant when enough cracks are opening. The effect of shear parameter is substantial here: decreasing its value from 1 to 0.65 doubles the peak stress. Thus, two extreme modes of model behaviour with respect to this parameter can be identified.

33

The first is given by value $\beta = 0$ which allows an infinite shear component for the traction vector resulting in an infinite compressive strength in uniaxial compression test. The second is given by increasing β infinitely which allows no shear at all resulting in a zero compressive strength in uniaxial compression test.

As for the predicted failure modes, they exhibit the typical slightly inclined localization bands. Moreover, the reduced shear contribution results in considerably wider localization bands, as can be observed in Figure 7c. The nature of these failure modes is mixed mode-I/II failure.

Discussion and conclusions

A rate-dependent multiple embedded discontinuity model was developed to simulate quasi-brittle fracture within the finite elements context. In the present approach, the discontinuities were pre-embedded (before the analysis) into each finite element of the mesh resulting in a formulation similar (in certain respects) to the classical interface or cohesive zone elements. However, the present approach is simpler and more efficient than the cohesive zone approach since neither duplication of mesh nodes nor contact interfaces (upon crack closure) are needed.

The presented method is simple having relatively small number (7 in total) of model parameters. The shear parameter controlling the interaction between the tensile and shear modes of fracture has a substantial effect on the compressive strength and the failure modes predicted with the model. By adjusting the tensile strength and the shear control parameter, the model can predict the correct tensile and compressive strengths as well as realistic failure modes of a quasi-brittle material such as rock in tension and uniaxial compression, as was shown in the numerical simulations.

As for the mesh dependency of the results predicted with the present method, it should be noted that there are two localization limiters of different nature in the present model. The first is provided by the embedded discontinuity method which is known to be mesh independent. The second is provided by the inclusion of viscosity in the model. Therefore, the results should be, in principle, mesh independent. However, further investigations on this issue are postponed to the future studies of the present method.

References

[1] T. Rabczuk. Computational Methods for Fracture in Brittle and Quasi-Brittle Solids: State-of-the-Art Review and Future Perspectives. *ISRN Applied Mathematics*, Article ID 849231, 2013. http://dx.doi.org/10.1155/2013/849231

[2] J.C. Simo, J. Oliver, F. Armero. An analysis of strong discontinuities induced by strain-softening in rate-independent inelastic solids. *Computational Mechanics*, 12:277-296, 1993.

[3] J.C. Simo, J. Oliver. A new approach to the analysis and simulation of strain softening in solids, in: Z.P. Bazant et al. (Eds.), Fracture and Damage in Quasi-brittle Structures, E. and F.N. Spon, London, 1994, pp. 25–39.

[4] J. Oliver. Modelling strong discontinuities in solid mechanics via strain softening constitutive equations. Parts 1: fundamentals. *International Journal for Numerical*

Methods in Engineering, 39:3575–3600, 1996. doi:10.1002/(SICI)1097-0207(19961115)39:21<3575::AID-NME65>3.0.CO;2-E

[5] J. Oliver. Modelling strong discontinuities in solid mechanics via strain softening constitutive equations. Part 2: numerical simulation. *International Journal for Numerical Methods in Engineering*; 39:3601–3623, 1996. doi: 10.1002/(SICI)1097-0207(19961115)39:21<3601::AID-NME64>3.0.CO;2-4

[6] T. Saksala. Rate-Dependent Embedded Discontinuity Approach Incorporating Heterogeneity for Numerical Modeling of Rock Fracture. *Rock Mechanics and Rock Engineering*, 48:1605–1622, 2015. doi:10.1007/s00603-014-0652-3

[7] N. Moës, J. Dolbow, T. Belytschko. A finite element method for crack growth without remeshing. *International Journal for Numerical Methods in Engineering*, 46:131-150, 1999. doi:10.1002/(SICI)1097-0207(19990910)46:1<131::AID-NME726>3.0.CO;2-J

[8] R. Radulovic, O.T. Bruhns, J. Mosler. Effective 3D failure simulations by combining the advantages of embedded Strong Discontinuity Approaches and classical interface elements. *Engineering Fracture Mechanics*, 78: 2470-2485, 2011. doi:10.1016/j.engfracmech.2011.06.007

[9] J. Mosler. On advanced solution strategies to overcome locking effects in strong discontinuity approaches. *International Journal for Numerical Methods in Engineering*, 63:1313-1341, 2005. doi: 10.1002/nme.1329

[10] O.M. Mahabadi. Investigating the influence of micro-scale heterogeneity and microstructure on the failure and mechanical behaviour of geomaterials. PhD Thesis, Graduate Department of Civil Engineering, University of Toronto, 2012.

Timo Saksala
Tampere University of Technology
Department of Civil Engineering
P.O. Box 600, FI-33101, Tampere, Finland
timo.saksala@tut.fi